Check for updates

ADVANCED MATERIALS
www.advmat.de

Extremely Robust and Multifunctional Nanocomposite Fibers for Strain-Unperturbed Textile Electronics

Jianfeng Gu, Fengchao Li, Yinbo Zhu, Donghui Li, Xue Liu, Bao Wu, Heng-An Wu, Xiangqian Fan, Xinyi Ji, Yongsheng Chen, and Jiajie Liang**

Textile electronics are needed that can achieve strain-unaltered performance when they undergo irregular and repeated strain deformation. Such strain-unaltered textile electronics require advanced fibers that simultaneously have high functionalities and extreme robustness as fabric materials. Current synthetic nanocomposite fibers based on inorganic matrix have remarkable functionalities but often suffer from low robustness and poor tolerance against crack formation. Here, we present a design for a high-performance multifunctional nanocomposite fiber that is mechanically and electrically robust, which was realized by crosslinking titanium carbide (MXene) nanosheets with a slide-ring polyrotaxane to form an internal mechanically-interlocked network. This inorganic matrix nanocomposite fiber featured distinct strain-hardening mechanical behavior and exceptional load-bearing capability (toughness approaching 60 MJ m^{-3} and ductility over 27%). It retained 100% of its ductility after cyclic strain loading. Moreover, the high electrical conductivity (>1.1×10^5 S m^{-1}) and electrochemical performance (>360 F cm^{-3}) of the nanocomposite fiber can be well retained after subjecting the fiber to extensive (>25% strain) and long-term repeated (10 000 cycles) dimensional changes. Such superior robustness allowed for the fabrication of the nanocomposite fibers into various robust wearable devices, such as textile-based electromechanical sensors with strain-unalterable sensing performance and fiber-shaped supercapacitors with invariant electrochemical performance for 10 000 strain loading cycles.

1. Introduction

Textile electronics made from fiber materials, ranging from traditional fiber materials to advanced functional fibers, have emerged as a next-generation technology that may find significant applications in applications where bendability, stretchability, wearability, portability, and lightness are needed.[1–3] Advanced fibers with integrated functionalities (i.e., conductivity) are of great interest for achieving wearable high-performance textile fabrics. Robustness, a rare yet important property allowing a system to maintain a stable structure and function against uncertainty perturbations, is highly required for wearable textile electronics.[4,5] In practical use, textile electronics are generally conformably attached or worn on the human body. Human motion is accompanied by irregular skin deformations that inevitably stretch or bend the textile electronics. Thus, robust textile electronics must function unalterably when disturbed by variable strain or stress.[6–8] To this end, functional fibers with intrinsically high robustness and multifunctionality may provide advanced fabric materials for achieving textile electronics with strain-unperturbed performance. However, achieving high-performance multifunctional fibers with high structural robustness and high damage resistance against strain remains a grand challenge.[3,9,10]

From the viewpoint of material science, the robustness and multifunctionality of synthetic fibers are usually mutually

J. Gu, F. Li, D. Li, X. Liu, X. Fan, X. Ji, J. Liang
School of Materials Science and Engineering, National Institute for Advanced Materials
Nankai University
Tianjin 300350, P. R. China
E-mail: liang0909@nankai.edu.cn

Y. Zhu, B. Wu, H.-A. Wu
CAS Key Laboratory of Mechanical Behavior and Design of Materials, Department of Modern Mechanics, CAS Center for Excellence in Complex System Mechanics
University of Science and Technology of China
Hefei 230027, P. R. China
E-mail: wuha@ustc.edu.cn

The ORCID identification number(s) for the author(s) of this article can be found under https://doi.org/10.1002/adma.202209527.

Y. Chen, J. Liang
Key Laboratory of Functional Polymer Materials of Ministry of Education
College of Chemistry
Nankai University
Tianjin 300350, P. R. China

J. Liang
School of Materials Science and Engineering, Smart Sensing Interdisciplinary Science Center
Nankai University
Tianjin 300350, P. R. China

DOI: 10.1002/adma.202209527

 © 2023 Wiley-VCH GmbH

15214095, 2023, 15, Downloaded from https://onlinelibrary.wiley.com/doi/10.1002/adma.202209527 by Nankai University, Wiley Online Library on [14/05/2023]. See the Terms and Conditions (https://onlinelibrary.wiley.com/terms-and-conditions) on Wiley Online Library for rules of use; OA articles are governed by the applicable Creative Commons License

exclusive. Previous studies have demonstrated mechanical robustness or high-performance functionalities, but synthetic fibers that combine these features remain elusive.[9–11] For fiber materials to be robust, current advanced fibers are typically made of tough polymer or polymeric composite with compliant structures that must be resistant to damage and resilient to large deformations.[12,13] However, such robust fibers usually have low or limited functionalities (i.e., low conductivity) due to the relatively low functionalities of the conventional polymer matrix, restricting their applications in textile electronics.[14,15] In contrast, synthetic nanocomposite fibers using functional inorganic or nanomaterials as the continuous phase, such as graphene and carbon nanotubes (CNTs), have demonstrated excellent functionalities.[16,17] Nevertheless, these fibrous structures with extensive internal interfaces or boundaries are usually irreversible, are naturally brittle, or have limited ductility; thus, they suffer from poor structural robustness and low tolerance against defect formation and propagation.[16–18] They are vulnerable to damage and cannot endure adverse conditions, such as large strain deformation or long-term cyclic strain loadings.[18,19] Thus, current advanced fiber materials typically possess either high device performance or high mechanical resilience, but it is hard to achieve both.

Here, we report a strategy for introducing a mechanically interlocked structure into a fibrous structure with functional nanomaterials as the continuous phase to achieve a high-performance multifunctional nanocomposite fiber with exceptional robustness against strain disturbance. The design of our robust and functional nanocomposite fiber included two main considerations. First, the main building blocks of the functional fibers should have intrinsically high mechanical properties and remarkable functionalities. It should also have a high aspect ratio to enable the formation of strong and high-performance fibers with large internal interfacial contacts for interface modifications. To achieve this, we utilized 2D titanium carbide $Ti_3C_2T_x$ (MXene) nanosheets as the matrix material due to their exceptional mechanical, electrical, structural, and chemical properties.[20–22] However, MXene matrix fibers typically have low ductility, low toughness, and poor robustness.[23,24] To overcome these issues, a mechanically interlocked polymer was introduced as the binder in the MXene fiber. A slide-ring polyrotaxane composed of a linear polymer guest (poly(ethylene glycol) (PEG)) threaded into multiple cyclic molecule hosts (α-cyclodextrin (α-CD)) is a typical mechanically interlocked polymer.[25–27] When the movable host molecules of the polyrotaxane were partially crosslinked with the matrix material, mechanically interlocked networks were formed.[25] The concentration of applied stress throughout the entire structure was minimized by adjusting the mechanically interlocked network (also named a "pulley" effect) when stretching the materials.[28] This endowed the structure with excellent mechanical adaptability and robustness against strain.[25] Thus, a slide-ring polyrotaxane was chosen as the intercalation material for our nanocomposite fiber due to its ability to form a mechanically-interlocked network.[25–27]

In this work, we report a high-performance multifunctional nanocomposite fiber from MXene nanosheets and a slide-ring polyrotaxane with exceptional robustness against strain disturbance. The MXene nanosheet matrix was crosslinked by the polyrotaxane to produce a mechanically interlocked structure inside the multilayered fibrous structure (**Figure 1**a),[26,27] which endowed our nanocomposite fiber with three superiorities. They included 1) outstanding multifunctionality, involving high electrical conductivity (over 1.1×10^5 S m^{-1}), high volumetric capacitance (over 360 F cm^{-3}), and high electromechanical performance; 2) exceptional load-bearing capability, featuring a strength of over 500 MPa, record-breaking ductility of over 27%, and high toughness of about 60 MJ m^{-3}; 3) distinct strain-hardening mechanical behavior enabling superior resistance to structural defect formation in the fiber even under large strain. As a result, the nanocomposite fibers maintained 100% of their mechanical ductility and electrical conductivity against large-strain deformation and long-term repeated (>10 000 cycles) strain loadings. Thus, they exhibited a high level of mechanical and electrical robustness not yet demonstrated before in inorganic-matrixed fiber materials. We used the nanocomposite fibers to fabricate wearable functional devices, including textile-based electromechanical sensors and fiber-shaped supercapacitors with desirable strain-unalterable functionalities, showing great promise for intelligent applications in emerging wearable technologies.

2. Results and Discussion

2.1. Material Design and Simulation

Employing a scalable and versatile wet-spinning assembly technology,[23,24] four types of MXene-based functional fibers were fabricated for comparison: pure MXene fiber, crosslinked MXene (cM) fiber, MXene/polyrotaxane (MP) fiber, and crosslinked MXene/polyrotaxane (cMP) nanocomposite fiber. $Ti_3C_2T_x$ MXene nanosheets (Figure S1, Supporting Information) were first mixed with slide-ring polyrotaxane with a glutamine transaminase stopper (Figure S2, Supporting Information) to form a viscous and thixotropic (Figure S3, Supporting Information) liquid crystal colloidal dispersion (Figure S4, Supporting Information). This dispersion tended to form long-range ordered nanosheet packing during the wet-spinning process.[23,24,29,30] MP fibers with different contents (5, 10, 15, 20, 25 wt%) of the polyrotaxane were fabricated by wet spinning in a coagulation bath, followed by hot stretching. The nanocomposite fibers compounded with 20 wt% of polyrotaxane achieved the best combination of strength, extensibility, and toughness, and thus were chosen to represent MP fiber for the following comparisons. The as-prepared MP fibers were soaked in crosslinking bath containing *N*,*N*′-carbonyldiimidazole (CDI), and Mg^{2+} to crosslink some of the α-CD components of polyrotaxane with MXene via the formation of ester bonds and ionic bonds to obtain cMP fibers with a mechanically interlocked structure (Figure 1b and Figure S5, Supporting Information). Four types of cMP fibers with different crosslinking states (designated as cMP-1 to cMP-4) were prepared, and cMP-3 fibers with optimal comprehensive performance were selected as representative cMP fibers for the following experiments. The exact polyrotaxane contents in cMP nanocomposite fibers were determined by thermogravimetric analysis (Figure S6, Supporting Information). The cM fibers without a polyrotaxane

 © 2023 Wiley-VCH GmbH

15214095, 2023, 15, Downloaded from https://onlinelibrary.wiley.com/doi/10.1002/adma.202209527 by Nankai University, Wiley Online Library on [14/05/2023]. See the Terms and Conditions (https://onlinelibrary.wiley.com/terms-and-conditions) on Wiley Online Library for rules of use; OA articles are governed by the applicable Creative Commons License

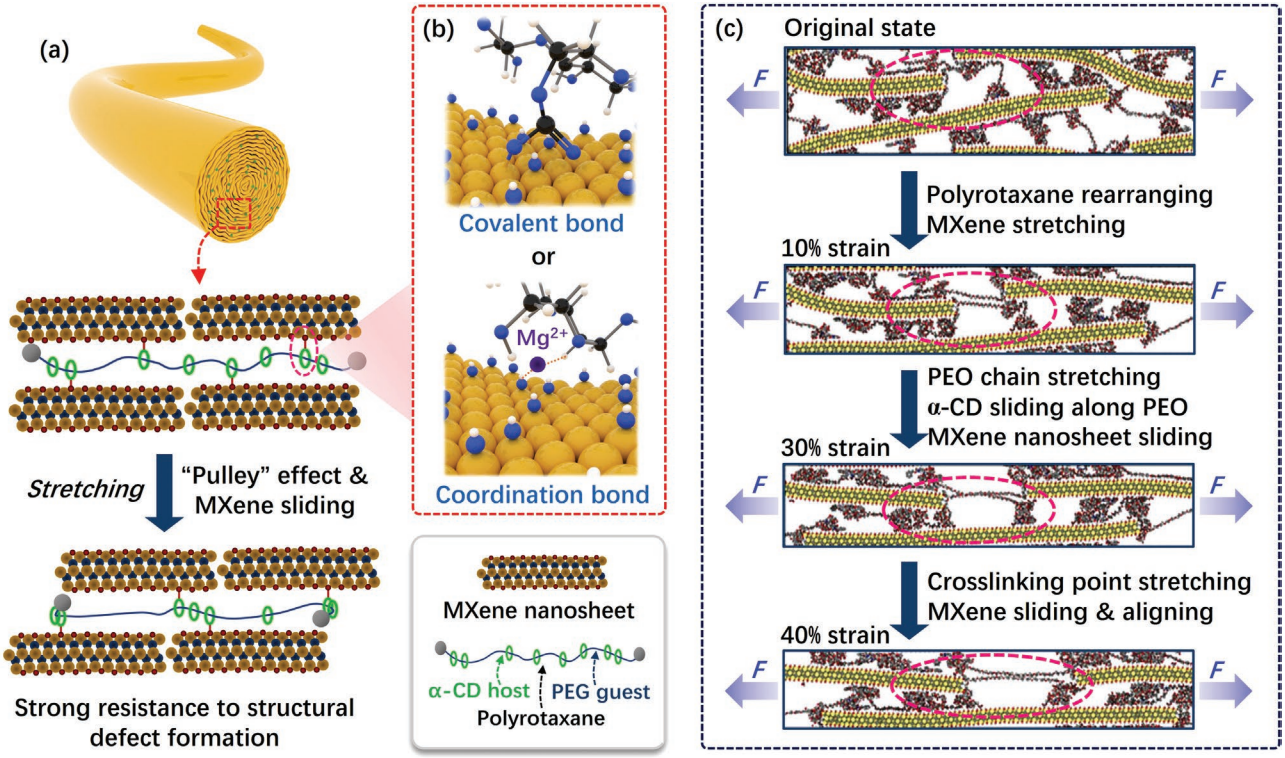

Figure 1. Schematic illustration and MD simulation of cMP fiber. a) Schematic illustration of the function of the mechanically interlocked structure that allows PEG main-chain stretching, α-CD ring slipping along the PEG main chain in polyrotaxane, and MXene nanosheet sliding over each other along the axial direction under tensile strain. b) The crosslinking points of covalent bonds and coordination bonds formed between MXene nanosheets and α-CD rings in the mechanically interlocked structure. c) MD simulation of the structurally robust mechanism of the cMP fibers under different strain states enabled by the mechanically interlocked structure.

were prepared using the same crosslinking conditions as the cMP-3 fibers (Figure S7, Supporting Information).

To evaluate how the mechanically interlocked structure influenced the structural robustness of cMP fibers against strain, a molecular dynamics (MD) model was used to simulate the tensile process of the nanocomposite fibers along the axial direction (Figure 1c; Note 3, Figures S8 and S9, Video S1, Supporting Information). It is interesting to note that the simulated stress–strain curve for cMP fiber exhibited distinctive non-linear mechanical behavior: a strain-softening phase (r-shape) before the yield point and a strain-hardening phase (J-shape) after the yield point (Figure S9b, Supporting Information). When stretching the nanocomposite fiber to below 10% strain, some hydrogen bonds between MXene nanosheets were first cleaved, accompanied by the rearrangement of polyrotaxane chains (Figure 1c and region I in Figure S9b, Supporting Information).[28] In this region, the sliding of α-CD rings in the polyrotaxane reduced the applied stress to some degree.[28] Upon further stretching the simulated fiber to about 30% strain (Figure 1c and region II and III in Figure S9b, Supporting Information), the "pulley effect" from the mechanically interlocked structure played the dominant role in releasing stress (Figure S9, Supporting Information).[28] The applied stress was first released by the further stretching of PEG chains and the ring sliding of the α-CD rings (Figure 1c and region II in Figure S9b, Supporting Information). This resulted in oscillating stress–strain behavior in which the average stress increased slightly within a large tensile strain (region II in Figure S9b, Supporting Information). The straightened polyrotaxane chains worked as molecular-scale bridges among MXene nanosheets via crosslinking points between α-CD rings and MXene. This triggered the mechanically interlocked network to transfer the applied stress to MXene nanosheets and thus promoted significant slippage and subsequent better alignment of MXene nanosheets along the stretching direction (Figure 1c and region III in Figure S9b, Supporting Information). These synergistic effects rapidly increased the tensile stress under further tension (region III in Figure S9b, Supporting Information), and maintained the structural integrity of the cMP fiber over tensile large strain without breaking. This simulation result clearly demonstrates that the mechanically interlocked structure played an important role in preserving the structural integrity of cMP fiber over a wide strain range.

2.2. Structure Characterization

Meter-long cMP fibers (**Figure 2**a) with an average diameter of 50 µm and wrinkled surface (Figure S10, Supporting Information) were produced via our scalable fabrication process. To confirm the formation of mechanically interlocked structure with covalent and ionic crosslinking points between MXene and polyrotaxane in the cMP fiber, the nanocomposite fiber was characterized by X-ray diffraction (XRD, Figure S11, Supporting

 © 2023 Wiley-VCH GmbH

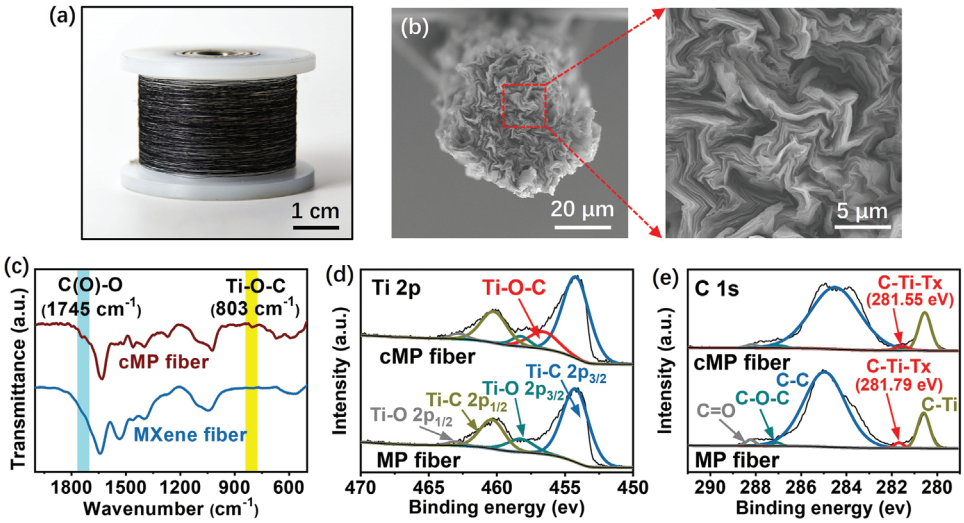

Figure 2. Characterization of cMP fiber. a) Photograph of the as-prepared meter-long cMP fiber wound on a drum. b) SEM images of the brittle fractured cross-sections of cMP fibers. c) Comparisons of FT-IR spectra for pure MXene and cMP fibers. d,e) XPS spectrum of cMP and MP fibers in the Ti 2p region (d) and the C 1s region (e).

Information), Fourier-transform infrared (FT-IR) spectroscopy (Figure 2c), and X-ray photoelectron spectroscopy (XPS, Figure 2d,e). The XRD patterns showed that the d-spacing increased from 1.27 nm for pure MXene fibers to 1.75 nm for cMP fibers (Figure S11a, Supporting Information), suggesting the intercalation of polyrotaxane into the MXene interlayers.[22] The d-spacing of cMP fiber decreased to 1.56 nm after stretching to 15% strain, indicating that the packed structure became denser after stretching (Figure S11b, Supporting Information). Two new peaks at 1745 cm^{-1} and 803 cm^{-1} ascribed to ester stretching and a Ti—O—C bond appeared in the FT-IR spectra of the cMP fibers (Figure 2c).[20,28] Moreover, a new peak at a binding energy of 456.6 eV due to Ti—O—C bond appeared in the XPS spectrum of the cMP fibers (Figure 2d).[20] These indicate the successful crosslinking of the hydroxyl groups of the α-CD unit of the polyrotaxane with the Ti—OH groups of MXene via CDI (Figure S5, Supporting Information).[26] Compared to pure MXene fiber, the C 1*s* peak corresponding to the C—Ti—T_x groups in cMP fibers slightly shifted from 281.79 to 281.55 eV (Figure 2e), probably due to the formation of ionic bonds between Mg^{2+} and Ti—OH groups in MXene (Figure S5, Supporting Information).[31,32]

The cross-sectional scanning electron microscopy (SEM) images of the brittle fracture surface of pure MXene and cM fibers showed numerous microvoids in their layered fibrous structures (Figure S12, Supporting Information). After intercalating polyrotaxane, there were many fewer and smaller microvoids in the MP fiber than in MXene and cM fibers (Figure S12, Supporting Information). Because of the synergistic densification effect caused by polyrotaxane insertion and crosslinking, microvoids were hardly visible in the cross-section of cMP fibers (Figure 2b). This densely packed multilayered structure guaranteed that the cMP fibers preserved a high conductivity up to 1106.5 ± 68.7 S cm^{-1} despite the presence of insulating polyrotaxane (Figure S13, Supporting Information).[21,33] This electrical property is lower than previously reported pure MXene fibers, is comparable to previously reported MXene-based composite fibers, and surpasses most graphene and CNT fibers (Table S2, Supporting Information).[19,34]

2.3. Exceptional Mechanical Properties

The impact of the mechanically interlocked structure was revealed by evaluating the mechanical properties of MXene, cM, MP, and cMP fibers and comparing their tensile stress–strain curves in **Figure 3**a. The MXene, cM, and MP fibers all exhibited plastic deformation and r-shaped curves in their stress-strain plots. This indicates typical strain-softening behavior that has been widely observed in conventional MXene, graphene, and CNT-based functional fibers due to inelastic deformation during inner interfacial slipping.[20,23] Both the MXene and cM fibers without a polyrotaxane displayed a limited tensile strength and ductility (Figure S14, Supporting Information). It is anticipated that the rupture of both types of fibers was caused by localized interfacial failure between MXene nanosheets.[19] In comparison, the ultimate elongation of MP fibers increased to 18.1 ± 0.6%, leading to a concurrent enhancement in the toughness to 21.9 ± 1.8 MJ m^{-3} (Figure S15, Supporting Information). This toughening behavior primarily resulted from the easy stretching of the polyrotaxane chains, which led to slippage of the MXene nanosheets to release stress.[35] However, compared with MXene fibers, the tensile strength of MP fibers only slightly increased to 188.7 ± 1.9 MPa. This was because the interfacial interactions between adjacent MXene nanosheets in MP fibers were dominated by weak hydrogen bonds. The pulley effect was negligible due to the lack of a mechanically interlocked network in the MP fibers.[28]

After crosslinking the MXene nanosheets with polyrotaxane to form a mechanically interlocked structure, the cMP fiber exhibited a distinctive nonlinear stress response to stress that involved softening before a critical strain and substantial hardening until failure at large strain (Figure 2a). This is consistent with the simulated result (Figure S9b, Supporting

© 2023 Wiley-VCH GmbH

15214095, 2023, 15, Downloaded from https://onlinelibrary.wiley.com/doi/10.1002/adma.202209527 by Nankai University, Wiley Online Library on [14/05/2023]. See the Terms and Conditions (https://onlinelibrary.wiley.com/terms-and-conditions) on Wiley Online Library for rules of use; OA articles are governed by the applicable Creative Commons License

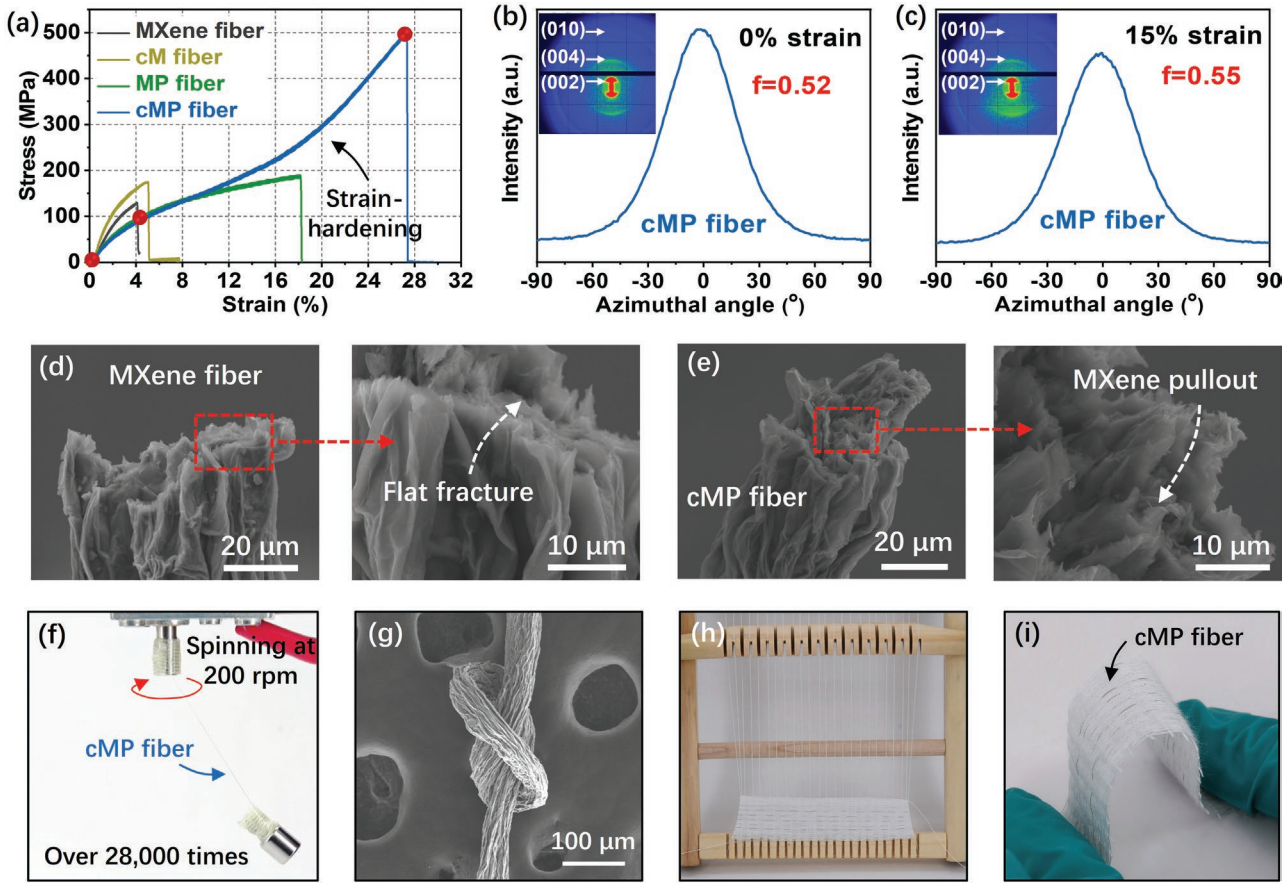

Figure 3. Mechanical properties of cMP fiber. a) Typical stress–strain curves of MXene, cM, MP, and cMP fibers. Only the curve of the cMP nanocomposite fibers showed strain-hardening behavior. b,c) 2D WAXS scattering patterns and azimuthal scanning profiles at the (002) peak for cMP fibers in the unstretched state (b) and under 15% tensile strain (c). d,e) SEM lateral views of the fracture surface of MXene fibers (d) and cMP fibers (e) after tensile tests. f) Photograph of a cMP fiber 5 cm long lifting a load more than 28 000 times greater than its own weight and spinning at 200 rpm. g) SEM image of a tightly knotted cMP fiber. h) Photograph showing cMP fibers weaved into textiles with commercial Nylon fibers using a knitting machine. i) Photograph of a cMP fiber-based flexible textile.

Information). Strain-hardening behavior has also been found in supertough elastomers crosslinked by slide-ring materials,[28] natural spider silks,[36,37] and animal hairs,[38] but it has never been observed in nanocomposite fibers with inorganic or nanomaterials as the continuous phase. Different from the typical nonlinear softening that leads to unrecoverable plastic deformation after the yield point, nonlinear hardening can ensure a high elasticity and thus high structure recovery during repeated stretching cycles.[39,40] Moreover, the strain-hardening behavior (less stress accumulation upon increasing the strain) led to fewer fractures and more crack propagation resistance in the fiber structure. This prevented damage from excessive strain and contributed to structural robustness.[39,40] Benefiting from the strain-hardening behavior, the cMP fibers exhibit a high load-bearing capacity characterized by multiple mechanical properties (Figure S16, Supporting Information), including a tensile strength of 502.3 ± 13.6 MPa, ductility of 27.3 ± 1.3%, and toughness of 59.7 ± 3.6 MJ m^{-3}, which were 3.9, 6.7, and 15.7 times higher than those of pure MXene fibers, respectively (Figure S17, Supporting Information). The ductility of the cMP fibers set a record compared with reported functional nanocomposite fibers.[23,24,34] Moreover, the obtained toughness of the cMP fibers was far superior to those of previously reported synthetic nanocomposite fibers, including MXene,[20,23,24] graphene,[19,41] and CNT-based fibers[42] (Table S2, Supporting Information).

2D small-angle/wide-angle X-ray scattering (SAXS/WAXS) measurements (Figure 3b,c, Figure S18, Supporting Information) and polarized Raman spectroscopy (Figure S19, Supporting Information) were performed to elucidate the structure change in cMP fibers during the tensile process. The Herman orientation factor (*f*), calculated from the azimuthal scan along the (002) peak measured in WAXS patterns,[30,43] increased from 0.52 in the unstretched state to 0.55 under 15% strain for cMP fibers (Figure 3b,c). This is indicative of a better orientation of MXenes along the fiber axial direction under stretching.[43] Polarized Raman spectroscopy also confirmed that the alignment degree of MXenes in the cMP fiber increased in the stretched state, as the intensity ratio of the G band for light polarized in the direction of the fiber axis to that for transverse polarization increased from 0.45 for cMP fibers in the original state to 1.02 under 15% strain (Figure S19, Supporting Information).[44,45] Consistent with the MD simulation results (Figure 1c), the mechanically interlocked structure promoted

© 2023 Wiley-VCH GmbH

15214095, 2023, 15, Downloaded from https://onlinelibrary.wiley.com/doi/10.1002/adma.202209527 by Nankai University, Wiley Online Library on [14/05/2023]. See the Terms and Conditions (https://onlinelibrary.wiley.com/terms-and-conditions) on Wiley Online Library for rules of use; OA articles are governed by the applicable Creative Commons License

the alignment of MXene nanosheets instead of crack or defect formation in the fiber during stretching. The lateral views of the fracture surface for MXene and cMP fibers are also shown in the SEM images (Figure 3d,e). In contrast to the flat and smooth fracture morphology of the MXene fiber (Figure 3d), a large extent of the pullout of MXene nanosheets with curled edges can be clearly observed in the fracture surface of cMP fiber (Figure 3e). This verifies that adjacent MXene nanosheets can slide over one another to a great degree in the cMP fiber to dissipate significant amounts of energy,[20] preventing structural defect formation and propagation.

The excellent load-bearing capability enabled a 5 cm-long cMP fiber to lift a load more than 28 000 times greater than its own weight and spin at 200 rpm without breaking (Figure 3f and Video S2, Supporting Information). The excellent ductility allowed the cMP fiber to be tightly knotted without breaking or cracking (Figure 3g). Moreover, the cMP fibers could be knitted into wearable textile electronics with commercial Nylon fibers using a knitting machine in a scalable way (Figure 3h,i, and Figure S20, Supporting Information). The fabrication process of textile electronics based on cMP fibers is detailed in Note 1, Supporting Information. The soft polymer fibers can provide the physiological comfort required by the wearer, while the cMP fibers can work as functional devices. Moreover, the washing durability of the textile based on cMP fibers was evaluated. After coating with a PDMS shell layer, the cMP fibers, which were knitted into a wearable textile with commercial Nylon fibers, were subjected to multiple washing–drying cycles. The electrical conductivity of the cMP fibers remained highly stable after 50 washing–drying cycles (Figure S21, Supporting Information).

2.4. Mechanical and Electrical Robustness

Next, to explore the mechanical and electrical robustness of cMP fiber, we measured the mechanical properties and electrical conductivity of the nanocomposite fibers after subjecting them to extensive and long-term cyclic dimensional changes. As shown in **Figure 4**a–c, the cMP fibers were first stretched to a specific strain, and a cyclic 1% strain loading was applied to the stretched nanocomposite fibers. The cMP fibers after a cyclic

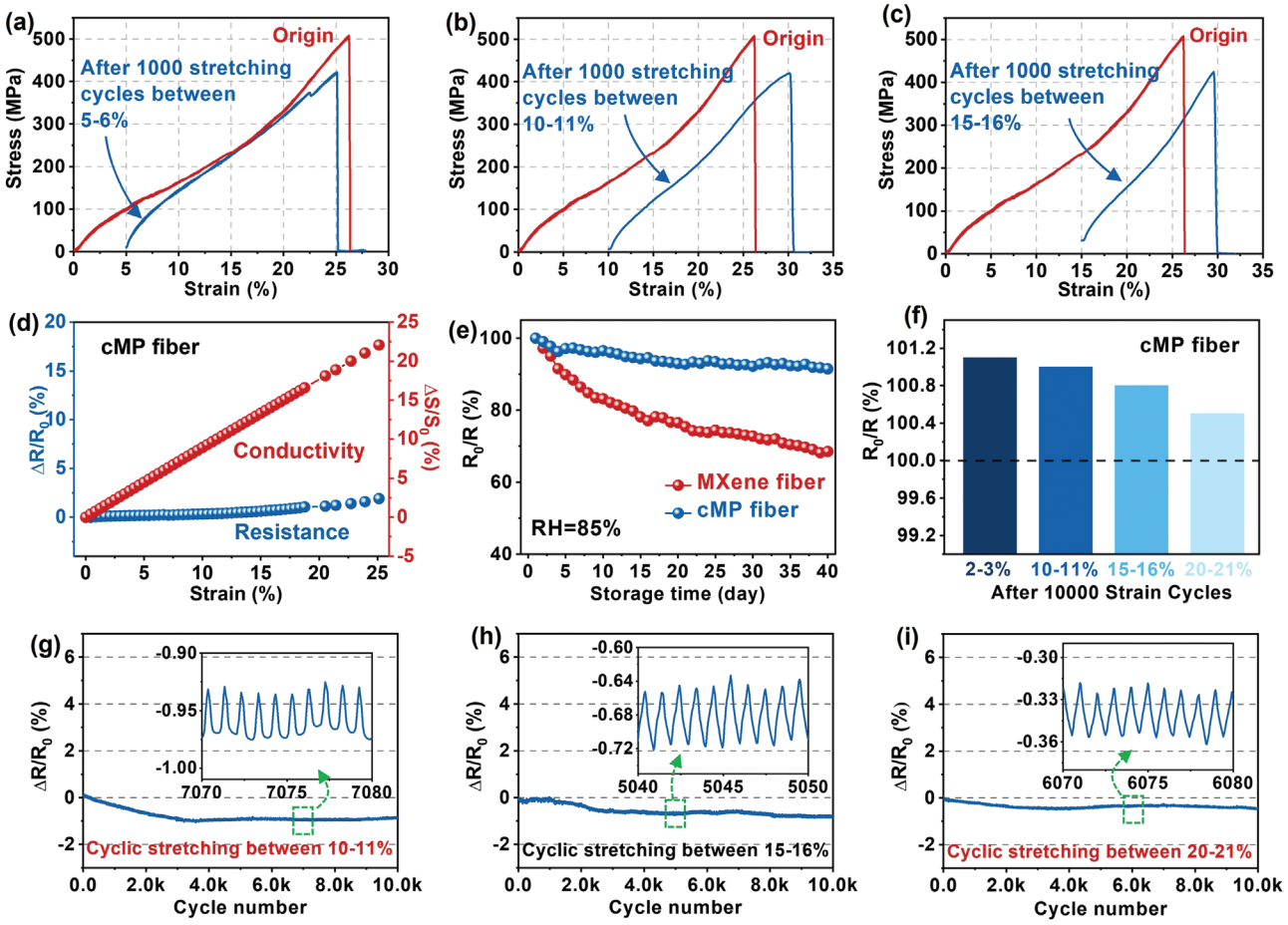

Figure 4. Mechanical and electrical robustness of cMP fiber. a–c) The stress–strain curves for cMP fibers measured after 1000 cycles of strain loading between 5–6% (a), 10–11% (b), and 15–16% (c), respectively. d) Conductivity and resistance change as a function of tensile strain for cMP fibers. e) Conductance retention percentages for pure MXene and cMP fibers over 30 days of storage at 20 °C and RH of 85%. f) Conductance retention percentages of cMP fibers after repeated 2–3%, 10–11%, 15–16%, and 20–21% strain for 10 000 stretch-release cycles, respectively. g–i) Relative resistance changes of the cMP fibers over 10 000 stretch-release cycles between 10–11% (g), 15–16% (h), and 20–21% (i) strain, respectively.

© 2023 Wiley-VCH GmbH

15214095, 2023, 15, Downloaded from https://onlinelibrary.wiley.com/doi/10.1002/adma.202209527 by Nankai University, Wiley Online Library on [14/05/2023]. See the Terms and Conditions (https://onlinelibrary.wiley.com/terms-and-conditions) on Wiley Online Library for rules of use; OA articles are governed by the applicable Creative Commons License

15214095, 2023, 15, Downloaded from https://onlinelibrary.wiley.com/doi/10.1002/adma.202209527 by Nankai University, Wiley Online Library on [14/05/2023]. See the Terms and Conditions (https://onlinelibrary.wiley.com/terms-and-conditions) on Wiley Online Library for rules of use; OA articles are governed by the applicable Creative Commons License

stretch-release test were further subjected to a tensile test. The ultimate tensile strength for those cMP fibers remained over 400 MPa (more than 80% strength retention) after 1000 strain loading cycles between 5–6%, 10–11%, and 15–16%, respectively (Figure 4a–c). Importantly, after cyclic strain loading, the cMP fibers could still be stretched to a failure strain of over 30% (Figure 4b,c), corresponding to about 100% retention of ductility. All of the above results indicate the superior mechanical robustness of our cMP fiber against strain disturbance.

Moreover, as shown in Figure 4a, only a tiny increase in resistance by 1.9% under 25% strain was observed in the stretched cMP fiber. The corresponding conductivity of cMP fibers under stretching showed a distinctive increase from 1100 to 1350 S cm^{-1} at 25% strain (Figure 4d). This increase in conductivity corresponded with the increase in the alignment degree of MXene nanosheets in cMP fibers along the stretching direction (Figure 3b,c, and Figure S19, Supporting Information) and the decrease in layer distance (Figure S11b, Supporting Information), which can lead to the formation of more conductive pathways in the fiber (Note 4 and Figure S23, Supporting Information).[21,46–48] Electrical resistance changes were further monitored when the cMP fibers underwent long-term cyclic strain loadings (Figure 4g–i). A slight decrease, rather than an increase, in the electrical resistance and an increase in conductivity were observed in cMP fibers after 10 000 stretch–release cycles between 10–11%, 15–16%, and 20–21% strain (Figure 4f), respectively, showing unprecedented fatigue resistance and electrical robustness. The peak and valley values of the relative resistance change showed small fluctuations during 10 stretch-release cycles between 0 and 25% strain (Figure S22, Supporting Information). This was because the cMP fiber underwent plastic deformation and could not fully recover to its original shape after being stretched to a large strain due to its inorganic matrix. Although the cMP fiber exhibited plastic deformation after being stretched to a large stain, it retained its high mechanical ductility and electrical conductivity, even in the unrelaxed state (Figure 4c,d) due to its excellent robustness and high tolerance against crack formation.

The embedding of the polyrotaxane in the interlayer spacings of MXene nanosheets also helped prevent the penetration of oxygen and water into the fibers. Resistance changes of MXene and cMP fibers were monitored at 20 °C and relative humidity (RH) of 85% to evaluate their oxidation resistance. The cMP fibers exhibited a conductance retention of over 91% after storage for 40 days, which was much higher than that of pure MXene fiber (Figure 4e), indicating significantly improved oxidation resistance. All the above results reveal the superior mechanical, electrical, structural, and environmental robustness of our cMP fibers with mechanically interlocked structure, which ensure that the nanocomposite fibers can be incorporated into textile fabrication.

2.5. Demonstration of Robust Wearable Devices

To assess how the robust and functional cMP fiber performed in a real-world scenario, we first applied the nanocomposite fiber as a robust electromechanical sensing device in wearable electronic to monitor and discriminate tiny force signals from the human body under disturbance. In practical use, most existing wearable sensors have an inevitable limitation, which is the alteration of quantitative sensing performance and accuracy when the sensors are under irregular stretching or bending. Generally, human motions are accompanied by substantial skin deformations, which will inevitably stretch or bend the wearable sensors (**Figure 5**a).[7] Thus, strain-unperturbed and robust wearable sensors are highly desired. However, in a typical resistive-type strain sensor, a high sensitivity requires mechanical brittleness, resulting in a structural disconnect and crack formation under small strains in the sensing material.[32,49,50] In contrast, high mechanical robustness and stable sensing require high structural robustness to retain structural connections or morphological integrity to suppress crack or defect formation in the sensing material. Thus, conventional resistive-type strain sensors based on a crack-propagation mechanism tend to suffer from limited sensing stability and anti-interfere.[8] In comparison, the strain-sensing mechanism of the cMP fiber was dominated by the slipping and alignment of MXene nanosheets instead of crack or defect formation in the fiber during stretching due to the mechanically-interlocked network structure of the fiber. It is thus envisioned that the cMP fiber can work as a fiber-based strain sensor with high mechanical robustness against disturbance.

To explore the robustness of the strain-sensing performance against perturbations or stressors, we first measured resistance changes as a function of applied cyclic strain for cMP fiber under varying mechanical interferences (Note 2, Supporting Information). As shown in Figures S24–S27, Supporting Information, the cMP fiber exhibited excellent durability and strong robustness in terms of strain-sensing performance against various strain or stress perturbations. Next, the cMP fibers were knitted into wearable tactile sensors with commercial Nylon fibers (Figure S20, Supporting Information) that were attached or placed on a deformable human body to monitor physiological information under different stretching deformation states of human skin. The textile strain sensor was then worn on the wrist of a 25-year-old male volunteer to measure the pulse waveforms from the radial artery (Figure 5a,b, Figure S28, Supporting Information). The soft nature of Nylon fibers can help the wearable tactile sensor tightly contact soft human skin, allowing it to monitor tiny pulse signals precisely and stably. Continuous and stable waveforms were obtained with high fidelity, and all pulse wave characteristics followed the rhythm of a heartbeat at a normal stationary state (Figure 5b and Figure S29, Supporting Information). The textile strain sensor had a high anti-interference ability and could function well for real-time pulse monitoring, even when the wearable sensor was under various stretching and deforming states (Figures S30 and S31, Supporting Information). As shown in Figure 5c–f, the systolic upstroke time (UT), reflected wave transit time (RWTT), left ventricular ejection time (LVET), systolic–diastolic time (PPT), pulse wave velocity (PWV), and (stiffness index) SI values were calculated from the pulse pressure waveform (Note 5, Supporting Information).[51] These values were compared with reported reference values for healthy individuals, and they showed strong robustness and consistency whether the volunteer's hand was relaxed or bent. This reflects the sensor's strong resistance against external interference and disturbances,

 © 2023 Wiley-VCH GmbH

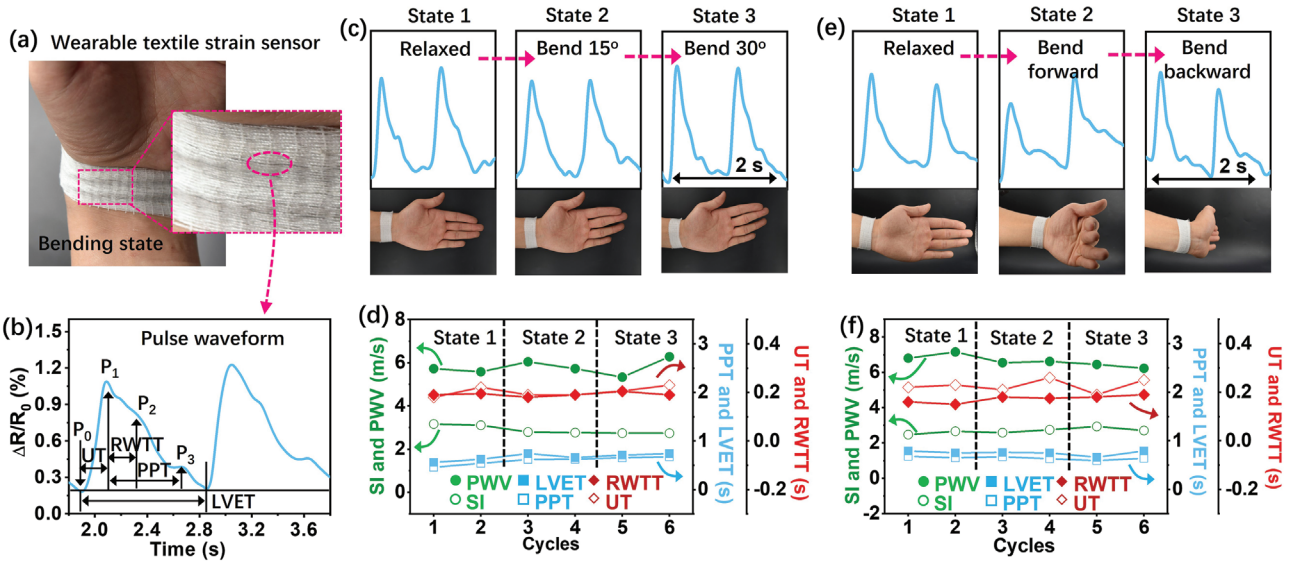

Figure 5. Demonstration of strain-unperturbed textile sensor. a) Photographs of a wearable cMP-fiber-based textile sensor wrapped onto a hand wrist to monitor human arterial pulse during wrist bending. The textile sensor deformed along with skin deformation during wrist bending. b) Typical contour plot of the measured arterial pulse waveforms from the cMP textile sensor wrapped around a wrist. c–f) The output waveforms of human arterial pulse were measured from cMP textile sensor under various wrist motions. c) A human wrist wearing a cMP textile sensor under different wrist motions: relaxed (state 1), bent 15° to the left (state 2), and bent 30° to the left (state 3), and the specific output waveform signals of two pulse cycles in the corresponding wrist bending states. d) The UT, RWTT, LVET, PPT, PWV, and SI values obtained from continuous pulse monitoring under different wrist bending states from (c). e) A human wrist wearing a cMP textile sensor under different wrist motion states: relaxed (state 1), bent forward (state 2), and bent backward (state 3) and the specific output waveform signals of two pulse cycles in the corresponding wrist bending states. f) The UT, RWTT, LVET, PPT, PWV, and SI values obtained from continuous pulse monitoring under different wrist motion states from (e). More than five samples were measured for each device.

which make our textile sensor promising for robust and strain-unperturbed wearable technology. In addition, this robust textile sensor can also be employed to precisely detect full-spectrum human motions, including the subtle strain of human body activities such as pulse, facial expressions, and phonation (Figure S32a,b, Supporting Information), and large human body movements such as human joint motion (Figure S32c,d, Supporting Information).

Next, we evaluated the electrochemical performance of our cMP fibers as supercapacitor electrodes in textile electronics against strain. To illuminate the kinetics of electron and ion transport of the cMP fiber electrode, electrochemical impedance spectroscopy (EIS) was first performed at a frequency range of 1 Hz to 1 M Hz. As shown in **Figure 6**a, the Nyquist plots for the cMP fiber electrode exhibited significant differences between the low-frequency and high-frequency regions relative to the pure MXene fiber. In the high-frequency region, the diameter of the semicircle for the cMP fiber was much smaller than that of pure MXene fiber, indicating that the charge transfer resistance was lower and the ionic conductivity was improved after embedding the polyrotaxane.[52] Moreover, the cMP fiber electrode showed a nearly vertical line in the low-frequency region, indicating a low ionic diffusion resistance. In contrast, the slope of the plots of the pure MXene fiber exhibited a nearly constant increase in the imaginary and real impedance, which indicates slow ion diffusion in its densely packed structure. The improved ion transport behavior in the cMP fiber was attributed to the embedded polyrotaxane within the PEG backbone, which provided more electrolyte-permeable active sites and ion diffusion channels.[53,54] In addition, negligible changes were observed in the Nyquist plots of the stretched cMP fiber electrode when the applied strain was varied from 0 to 25% in the tensile direction (Figure 6b).

To investigate the electrochemical performance of the cMP fibers, we also evaluated the fiber electrode in 1 M H_2SO_4 as an aqueous electrolyte, and the typical cyclic voltammetry (CV) curves measured from 5 to 100 mV s^{-1} scan rates are shown in Figure 6c. The cMP fiber electrode exhibited pseudocapacitive behavior and demonstrated a high volumetric capacitance of 362 F cm^{-3} at a scan rate of 5 mV s^{-1}. The long-term cycling stability of the cMP fiber tested at 20 A cm^{-3} showed that the fiber electrode was highly stable with almost 100% capacitance retention after 25 000 charging/discharging cycles (Figure 6d). In addition to its electrochemical performance, the cMP fiber electrode also exhibited stable electrochemical performance during stretching. Almost 100% capacitance was retained for the cMP fiber electrode over 25% tensile strain (Figure 6e). Moreover, the cMP fiber electrode showed invariant capacitance (100% retention) against cyclically applied tensile strain (over 10 000 cycles) between 5–6%, 10–11%, 15–16%, and 20–21%, respectively, as displayed in Figure 5f,g. In contrast, the pure MXene fiber electrode exhibited <70% capacitance retention after being subjected to 1000 stretching cycles between 2 and 3% strain (Figure S33, Supporting Information). Thus, the cMP fiber electrode exhibited robust electrochemical performance against strain disturbance.

To further evaluate the potential use of our cMP fiber in a full cell, we assembled a symmetric fiber-shaped supercapacitor

© 2023 Wiley-VCH GmbH

15214095, 2023, 15, Downloaded from https://onlinelibrary.wiley.com/doi/10.1002/adma.202209527 by Nankai University, Wiley Online Library on [14/05/2023]. See the Terms and Conditions (https://onlinelibrary.wiley.com/terms-and-conditions) on Wiley Online Library for rules of use; OA articles are governed by the applicable Creative Commons License

15214095, 2023, 15, Downloaded from https://onlinelibrary.wiley.com/doi/10.1002/adma.202209527 by Nankai University, Wiley Online Library on [14/05/2023]. See the Terms and Conditions (https://onlinelibrary.wiley.com/terms-and-conditions) on Wiley Online Library for rules of use; OA articles are governed by the applicable Creative Commons License

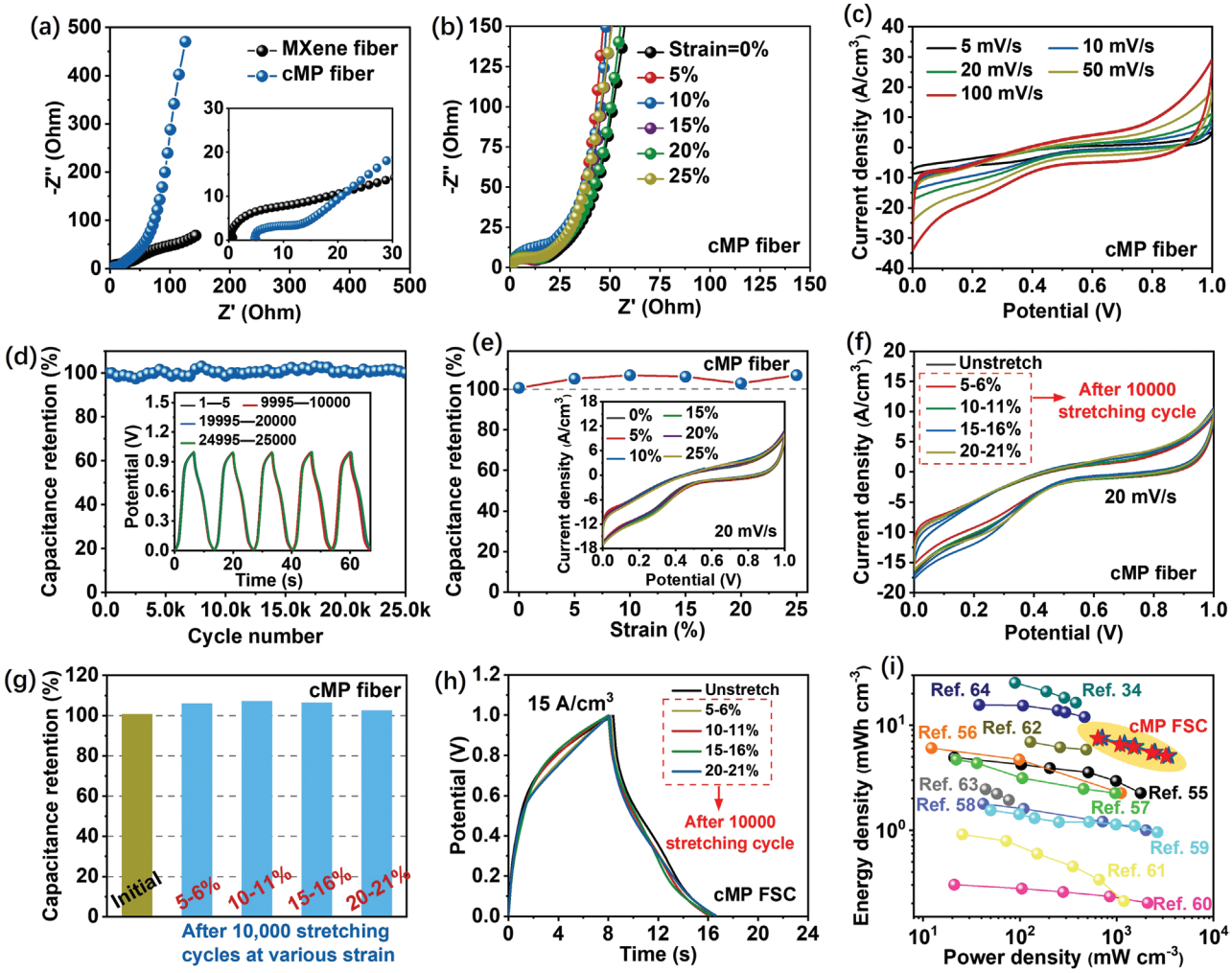

Figure 6. Robust electrochemical performance of cMP fiber and cMP fiber-based supercapacitor. a) Electrochemical impedance spectroscopy (EIS) data for cMP and pure MXene fiber. b) EIS data for cMP fiber under initial and stretched state at various strains. c) CV curves (from 5 to 100 mV s^{-1}) of the cMP fiber electrode. d) Capacitance retention during the cycling of a cMP fiber electrode. Inset shows the first to fifth, 9995th to 10 000th, 19 995th to 20 000th, and 24 995th to 25 000th cycles of the cMP fiber electrodes. e) Capacitance retention versus tensile strain for a cMP fiber electrode. Inset shows the CV curves at 20 mV s^{-1} for the cMP fiber electrode in the initial and stretched states at various strains. f) CV curves at 20 mV s^{-1} for the cMP fiber electrode in the initial state and after 10 000 stretching cycles between strains of 5–6%, 10–11%, 15–16%, and 20–21%, respectively. g) Capacitance retention of the cMP fiber electrode after 10 000 stretching cycles between strains of 5–6%, 10–11%, 15–16%, and 20–21%, respectively. h) Galvanostatic charge/discharge curves (at 15 A cm^{-3}) for the cMP fiber electrode after 10 000 stretching cycles between strains of 5–6%, 10–11%, 15–16%, and 20–21%, respectively. i) Volumetric energy density and power density of the cMP FSC in the initial state and after 10 000 stretching cycles between strains of 5–6%, 10–11%, 15–16%, and 20–21%, respectively, compared with state-of-the-art fiber-based supercapacitors.

(denoted as cMP FSC) by using cMP fibers as both the negative and positive fiber electrodes. Figure S34, Supporting Information illustrates the galvanostatic charge/discharge (GCD) curves of the cMP FSC at current densities ranging from 5 to 20 A cm^{-3}. Importantly, negligible changes were observed in the GCD curves under various current densities when the cMP FSC was subjected to 10 000 stretching cycles between strains of 5–6%, 10–11%, 15–16%, and 20–21% (Figure 6h and Figure S35, Supporting Information). Ragone plots related to volumetric energy and power densities of the cMP FSC after being subjected to cyclic strain loadings were compared to state-of-the-art fiber-shaped supercapacitors, as shown in Figure 6i. The cMP FSC exhibited high densities in the range of 5.2–7.6 mW cm^{-3} with corresponding power densities in the range of 3.4–0.7 W cm^{-3}. These values are superior to those of most reported fiber-shaped supercapacitors.[34,55–64] Most importantly, these volumetric energy and power density values were invariant for the cMP FSC, even when the fiber supercapacitor was repeatedly stretched for over 10 000 cycles at various strains (Figure 6i and Figure S36, Supporting Information), indicating robust electrochemical performance.

Finally, a wearable integrated system consisting of the cMP fiber sensor and cMP FSC was constructed by knitting a cMP fiber and two cMP FSCs (connected in series) with Nylon fibers (Figure S37a, Supporting Information). As an integrated textile electronic, the cMP FSCs provided efficient power (Figure S37b, Supporting Information) to the cMP fiber sensor to monitor human blowing (Figure S37c, Supporting Information) and

 © 2023 Wiley-VCH GmbH

15214095, 2023, 15, Downloaded from https://onlinelibrary.wiley.com/doi/10.1002/adma.202209527 by Nankai University, Wiley Online Library on [14/05/2023]. See the Terms and Conditions (https://onlinelibrary.wiley.com/terms-and-conditions) on Wiley Online Library for rules of use; OA articles are governed by the applicable Creative Commons License

detect the bending and relaxing of the finger joint (Figure S37d, Supporting Information). This indicates that our multifunctional cMP fibers could be harnessed simultaneously as a power source and functional device for wearable textile electronics.

3. Conclusion

We have achieved MXene matrixed nanocomposite fibers with both high multifunctionality and superior robustness by introducing a mechanically interlocked network inside the fibrous structure. This distinctive structure enhanced the interfacial interactions between MXene nanosheets, promoted the sliding and alignment of MXene nanosheets during tensile strain, and maintained the integrity of the fibrous structure over a wide strain range. As a result, the obtained nanocomposite fiber obtained strong resistance against structural crack formation and propagation, and thus, maintained its multifunctionality during cyclic strain perturbations or after being stretched to a large strain. The nanocomposite fibers were assembled into wearable textile electronics, including textile-based electromechanical sensors and fiber-shaped supercapacitors, which exhibited highly desirable strain-unalterable functionalities. Considering the mass production capabilities, remarkable mechanical properties, greatly improved chemical stability, good washing durability, and excellent multifunctionality, the cMP nanocomposite fiber showed great potential for a wide range of applications in next-generation wearable electronics.

4. Experimental Section

Raw Materials: Titanium aluminum carbide (Ti_3AlC_2) was purchased from 11 Technology Co., Ltd. (China). (2-Hydroxypropyl)-α-cyclodextrin (HP-α-CD) was purchased from Tianjin Bohua Chemical Reagent Co., Ltd. (Tianjin, China). Amino-terminated PEG (PEG-NH_2, M_w = 20 000) was purchased from Shanghai Yuanye Biotechnology Co., Ltd. (Shanghai, China). *N*-α-Carbobenzoxy-L-glutaminyl-glycine (Z-Gln-Gly) was purchased from Shanghai Bide Pharmaceutical Technology Co., Ltd. (Shanghai, China). Glutamine Transaminases (TGases) were purchased from Beijing Soleibo Technology Co., Ltd. (Beijing, China). Lithium fluoride (LiF), CDI, dimethyl sulfoxide (DMSO), and anhydrous magnesium sulfate ($MgSO_4$) were purchased from Beijing Inokay Technology Co., Ltd. (Beijing, China).

Synthesis of $Ti_3C_2T_x$ Nanosheets: MXene was obtained by the selective etching of Al atomic layers from a Ti_3AlC_2 MAX phase (400 mesh size) and delamination using the minimally-intensive layer delamination method. Here, 2 g of LiF was dissolved in 40 mL of 9 M hydrochloric acid and stirred for 30 min. Afterward, 2 g Ti_3AlC_2 powder was immersed in the solution and constantly stirred for 12 h at 35 °C. The Al layer in the MAX phase was etched for exfoliation of $Ti_3C_2T_x$. The obtained acidic solution was washed by repeated centrifugation at 3500 rpm for 10 min until its pH reached 5–6. The bottom layer of precipitated $Ti_3C_2T_x$ was dispersed in ethanol via ultrasonication for 30 min. Then, ethanol was removed by centrifugation at 10 000 rpm for another 30 min. In the next step, distilled water was added to the new precipitate and sonicated for 20 min. Then, the solution was again centrifuged at 3500 rpm. Finally, the resulting homogeneous MXene solution was freeze-dried to obtain MXene powder.

Synthesis of Polyrotaxane: The polyrotaxane was prepared using a one-pot method as shown in Figure S1, Supporting Information. HP-α-CD (1 g) was dissolved in 3 mL of phosphate buffer solution (PBS, 0.1 mol L^{-1}, pH 8.0). Then, 0.2 g of PEG-NH_2 was added and stirred for 1 h to obtain a clear solution, which was allowed to stand in a refrigerator at 4 °C for 36 h. Then, 0.08 g of Z-Gln-Gly and 10 mg of TGase were added to the mixture for end-capping. The reaction was stirred at room temperature for 3 d. The above mixture was dialyzed (molecular-weight cut-off (MWCO): 8000–14 000) for 48 h to remove free Z-Gln-Gly, HP-α-CD, and TGase. Then, the dialyzed solution was freeze-dried to obtain the rough product. The above product was dissolved in tetrahydrofuran and centrifuged at 3500 rpm for 10 min. Centrifugation was repeated three times to remove free PEG-NH_2 and then dialyzed again for 48 h. The dialyzed solution was filtrated through a 0.45 µm membrane filter and then freeze-dried to obtain a polyrotaxane with a low coverage.

Fabrication of Pure MXene Fiber: MXene nanosheets were dispersed in deionized water via sonication to make MXene colloidal suspension with a concentration of 150 mg mL^{-1}. MXene spinning solution (1 mL) was added to a 3 mL syringe (Becton Dickinson), and a 90° curved blunt needle (26 G) was fixed onto the syringe end. The spinning solution was extruded through the needle spinneret into the rotating coagulation bath (acetic acid, 99.5%) at a velocity of 5 mL h^{-1}. The resulting fibers were dried and stretched to different ratios under a 250 W lamp. Finally, all fibers were collected on reels and then placed in a glove box for 12 h before use.

Preparation of MP Fiber: First, polyrotaxane was dissolved in a small amount of deionized water. The polyrotaxane dispersion was then added to the MXene dispersion (150 mg mL^{-1}) and vortexed for 3 h at room temperature. Finally, the composite spinning solution was sonicated for 5 min and degassed for further use. The mass fractions of polyrotaxane in the composite spinning solution were 5, 10, 15, 20, and 25 wt%, respectively. The MXene/polyrotaxane spinning solution (1 mL) was added to a 3 mL syringe (Becton Dickinson), and a 90° curved blunt needle (26 G) was attached to the end of the syringe. The coagulation bath and spinning conditions of MP fibers were the same as those of pure MXene fibers. The resulting fibers were dried and stretched to a certain ratio under a 250 W lamp. Finally, all fibers were collected on reels and then placed in a glove box for 12 h before use.

Preparation of cMP Fibers: First, CDI was dissolved in 10 mL of DMSO to create solutions with different weight concentrations by stirring for 20 min. Then, $MgSO_4$ was added to the CDI/DMSO solutions to prepare the crosslinking bath. Four crosslinking baths based on DMSO solutions with different contents of CDI and $MgSO_4$ were prepared (Figure S15, Supporting Information): Bath-1 with 2.27 wt% CDI, Bath-2 with 2.27 wt% CDI and 0.32 wt% of $MgSO_4$, Bath-3 with 2.27 wt% CDI and 0.45 wt% of $MgSO_4$, and Bath-4 with 2.27 wt% CDI and 0.59 wt% of $MgSO_4$. The MXene/polyrotaxane spinning solution (1 mL) was added to a 3 mL syringe (Becton Dickinson), and a 90° curved blunt needle (26 G) was attached to the end of the syringe. The coagulation bath and spinning conditions of MP fibers were the same as those used for pure MXene fibers. The resulting fibers were dried and stretched to a certain ratio under a 250 W lamp. The fibers were then pasted in a ceramic mold, and the crosslinking bath solution was subsequently poured into the mold. After the fibers were crosslinked at 60 °C for 30 min, the crosslinking bath solution was poured out of the mold, and the fibers were washed with ethanol. Finally, the crosslinked fibers were vacuum-dried at 130 °C for 40 min. cMP-1, cMP-2, cMP-3, and cMP-4 represent cMP fibers soaked in Bath-1, Bath-2, Bath-3, and Bath-4 for crosslinking, respectively.

Preparation of cM Fibers: The pure MXene fibers were soaked in Bath-3 and crosslinked at 60 °C for 30 min, following the crosslinking conditions of the cMP-3 fibers. After crosslinking was complete, the crosslinking bath solution was poured out of the mold, and the fibers were washed with ethanol. Finally, the cM fibers were vacuum-dried at 130 °C for 40 min.

Supporting Information

Supporting Information is available from the Wiley Online Library or from the author.

 © 2023 Wiley-VCH GmbH

Acknowledgements

This work reported here was supported by the National Natural Science Fund of China (51872146, 52173238, 11872063, and 12172346), the Municipal Natural Science Fund of Tianjin (20JCJQJC00010), the National Key Research and Development Program of China (2021YFA0715700), the Fundamental Research Funds for the Central Universities of Nankai University (63191520), and the Youth Innovation Promotion Association CAS (2022465). To conduct the related human-motion detection experiments (pulse, voice, and limb movement) on the human body involved in this work, rules or permissions from the relevant national or local authorities are not in place in the country where the experiments were performed. The volunteers took part in this proof-of-concept illustration with the full understanding of the process and any risks involved. Informed written consent was obtained from the volunteers.

Conflict of Interest

The authors declare no conflict of interest.

Author Contributions

J.G., F.L., and Y.Z. contributed equally to this work. J.L. supervised the project, and conceived and designed the research. J.G., F.L., X.L., X.F., and X.J. participated in materials preparation, device fabrication, device test, or interpretation of results. Y.Z., B.W., and H.-A.W. performed the mechanical simulations and analyzations. J.G., Y.Z., and J.L. analyzed the data and co-wrote the manuscript. All authors analyzed and discussed the results.

Data Availability Statement

The data that support the findings of this study are available from the corresponding author upon reasonable request.

Keywords

functional fibers, MXenes, nanocomposite fibers, robustness, textile electronics

Received: October 16, 2022
Revised: December 19, 2022
Published online: March 4, 2023

[1] X. Shi, Y. Zuo, P. Zhai, J. Shen, Y. Yang, Z. Gao, M. Liao, J. Wu, J. Wang, X. Xu, Q. Tong, B. Zhang, B. Wang, X. Sun, L. Zhang, Q. Pei, D. Jin, P. Chen, H. Peng, *Nature* **2021**, *591*, 240.
[2] Z. Wen, M.-H. Yeh, H. Guo, J. Wang, Y. Zi, W. Xu, J. Deng, L. Zhu, X. Wang, C. Hu, L. Zhu, X. Sun, Z. Wang, *Sci. Adv.* **2016**, *2*, e1600097.
[3] L. Wang, X. Fu, J. He, X. Shi, T. Chen, P. Chen, B. Wang, H. Peng, *Adv. Mater.* **2020**, *32*, 1901971.
[4] Y. Liu, X. Zhou, H. Yan, Z. Zhu, X. Shi, Y. Peng, L. Chen, P. Chen, H. Peng, *Adv. Funct. Mater.* **2022**, *32*, 2201510.
[5] S. Zhu, M. Wang, Z. Qiang, J. Song, Y. Wang, Y. Fan, Z. You, Y. Liao, M. Zhu, C. Ye, *Chem. Eng. J.* **2021**, *406*, 127140.
[6] C. M. Ajmal, S. Cha, W. Kim, K. P. Faseela, H. Yang, S. Baik, *Sci. Adv.* **2022**, *8*, eabn3365.
[7] Q. Su, Q. Zou, Y. Li, Y. Chen, S. Teng, J. T. Kelleher, R. Nith, P. Cheng, N. Li, W. Liu, S. Dai, Y. Liu, A. Mazursky, J. Xu, L. Jin, P. Lopes, S. Wang, *Sci. Adv.* **2021**, *7*, eabi4563.
[8] O. A. Araromi, M. A. Graule, K. L. Dorsey, S. Castellanos, J. R. Foster, W. H. Hsu, A. E. Passy, J. J. Vlassak, J. C. Weaver, C. J. Walsh, R. J. Wood, *Nature* **2020**, *587*, 219.
[9] W. Weng, P. Chen, S. He, X. Sun, H. Peng, *Angew. Chem., Int. Ed.* **2016**, *55*, 6140.
[10] L. Veeramuthu, C. J. Cho, M. Venkatesan, G. R. Kumar, H.-Y. Hsu, B.-X. Zhuo, L.-J. Kau, M.-A. Chung, W.-Y. Lee, C.-C. Kuo, *Nano Energy* **2022**, *101*, 107592.
[11] B. Fang, D. Chang, Z. Xu, C. Gao, *Adv. Mater.* **2020**, *32*, 1902664.
[12] J. Song, S. Chen, L. Sun, Y. Guo, L. Zhang, S. Wang, H. Xuan, Q. Guan, Z. You, *Adv. Mater.* **2020**, *32*, 1906994.
[13] M. Yao, B. Wu, X. Feng, S. Sun, P. Wu, *Adv. Mater.* **2021**, *33*, 2103755.
[14] J. Guo, X. Liu, N. Jiang, A. K. Yetisen, H. Yuk, C. Yang, A. Khademhosseini, X. Zhao, S.-H. Yun, *Adv. Mater.* **2016**, *28*, 10244.
[15] J. Guo, B. Zhou, C. Yang, Q. Dai, L. Kong, *Adv. Funct. Mater.* **2019**, *29*, 1902898.
[16] G. Xin, T. Yao, H. Sun, S. M. Scott, D. Shao, G. Wang, J. Lian, *Science* **2015**, *349*, 1083.
[17] N. Behabtu, C. C. Young, D. E. Tsentalovich, O. Kleinerman, X. Wang, A. W. K. Ma, E. A. Bengio, R. F. ter Waarbeek, J. J. de Jong, R. E. Hoogerwerf, S. B. Fairchild, J. B. Ferguson, B. Maruyama, J. Kono, Y. Talmon, Y. Cohen, M. J. Otto, M. Pasquali, *Science* **2013**, *339*, 182.
[18] I. H. Kim, T. Yun, J.-E. Kim, H. Yu, S. P. Sasikala, K. E. Lee, S. H. Koo, H. Hwang, H. J. Jung, J. Y. Park, H. S. Jeong, S. O. Kim, *Adv. Mater.* **2018**, *30*, 1803267.
[19] Y. Zhang, J. Peng, M. Li, E. Saiz, S. E. Wolf, Q. Cheng, *ACS Nano* **2018**, *12*, 8901.
[20] T. Zhou, C. Wu, Y. Wang, A. P. Tomsia, M. Li, E. Saiz, S. Fang, R. H. Baughman, L. Jiang, Q. Cheng, *Nat. Commun.* **2020**, *11*, 2077.
[21] T. Zhou, Y. Yu, B. He, Z. Wang, T. Xiong, Z. Wang, Y. Liu, J. Xin, M. Qi, H. Zhang, X. Zhou, L. Gao, Q. Cheng, L. Wei, *Nat. Commun.* **2022**, *13*, 4564.
[22] X. Shi, X. Fan, Y. Zhu, Y. Liu, P. Wu, R. Jiang, B. Wu, H.-A. Wu, H. Zheng, J. Wang, X. Ji, Y. Chen, J. Liang, *Nat. Commun.* **2022**, *13*, 1119.
[23] S. Li, Z. Fan, G. Wu, Y. Shao, Z. Xia, C. Wei, F. Shen, X. Tong, J. Yu, K. Chen, M. Wang, Y. Zhao, Z. Luo, M. Jian, J. Sun, R. B. Kaner, Y. Shao, *ACS Nano* **2021**, *15*, 7821.
[24] W. Eom, H. Shin, R. B. Ambade, S. H. Lee, K. H. Lee, D. J. Kang, T. H. Han, *Nat. Commun.* **2020**, *11*, 2825.
[25] L. Chen, X. Sheng, G. Li, F. Huang, *Chem. Soc. Rev.* **2022**, *51*, 7046.
[26] L. Jiang, C. Liu, K. Mayumi, K. Kato, H. Yokoyama, K. Ito, *Chem. Mater.* **2018**, *30*, 5013.
[27] C. Liu, N. Morimoto, L. Jiang, S. Kawahara, T. Noritomi, H. Yokoyama, K. Mayumi, K. Ito, *Science* **2021**, *372*, 1078.
[28] S. Choi, T.-W. Kwon, A. Coskun, J. W. Choi, *Science* **2017**, *357*, 279.
[29] H. Park, K. H. Lee, Y. B. Kim, S. B. Ambade, S. H. Noh, W. Eom, J. Y. Hwang, W. J. Lee, J. Huang, T. H. Han, *Sci. Adv.* **2018**, *4*, eaau2104.
[30] J. Zhang, S. Uzun, S. Seyedin, P. A. Lynch, B. Akuzum, Z. Wang, S. Qin, M. Alhabeb, C. E. Shuck, W. Lei, E. C. Kumbur, W. Yang, X. Wang, G. Dion, J. M. Razal, Y. Gogotsi, *ACS Cent. Sci.* **2020**, *6*, 254.
[31] S. Wan, F. Xu, L. Jiang, Q. Cheng, *Adv. Funct. Mater.* **2017**, *27*, 1605636.
[32] X. Shi, H. Wang, X. Xie, Q. Xue, J. Zhang, S. Kang, C. Wang, J. Liang, Y. Chen, *ACS Nano* **2019**, *13*, 649.
[33] Z. Xu, C. Gao, *Nat. Commun.* **2011**, *2*, 571.
[34] Q. Liu, A. Zhao, X. He, Q. Li, J. Sun, Z. Lei, Z.-H. Liu, *Adv. Funct. Mater.* **2021**, *31*, 2010944.
[35] R. Du, Z. Xu, C. Zhu, Y. Jiang, H. Yan, H.-C. Wu, O. Vardoulis, Y. Cai, X. Zhu, Z. Bao, Q. Zhang, X. Jia, *Adv. Funct. Mater.* **2020**, *30*, 1907139.
[36] N. Du, Z. Yang, X. Liu, Y. Li, H. Xu, *Adv. Funct. Mater.* **2011**, *21*, 772.

© 2023 Wiley-VCH GmbH

15214095, 2023, 15, Downloaded from https://onlinelibrary.wiley.com/doi/10.1002/adma.202209527 by Nankai University, Wiley Online Library on [14/05/2023]. See the Terms and Conditions (https://onlinelibrary.wiley.com/terms-and-conditions) on Wiley Online Library for rules of use; OA articles are governed by the applicable Creative Commons License

[37] W. Zhang, C. Ye, K. Zheng, J. Zhong, Y. Tang, Y. Fan, M. J. Buehler, S. Ling, D. L. Kaplan, *ACS Nano* **2018**, *12*, 6968.
[38] W. Yang, Y. Yu, R. O. Ritchie, M. A. Meyers, *Matter* **2020**, *2*, 136.
[39] S. W. Cranford, A. Tarakanova, N. M. Pugno, M. J. Buehler, *Nature* **2012**, *482*, 72.
[40] Y. Ma, X. Feng, J. A. Rogers, Y. Huang, Y. Zhang, *Lab Chip* **2017**, *17*, 1689.
[41] Y. Zhang, Y. Li, P. Ming, Q. Zhang, T. Liu, L. Jiang, Q. Cheng, *Adv. Mater.* **2016**, *28*, 2834.
[42] G. Wang, S.-K. Kim, M. C. Wang, T. Zhai, S. Munukutla, G. S. Girolami, P. J. Sempsrott, S. Nam, P. V. Braun, J. W. Lyding, *ACS Nano* **2020**, *14*, 632.
[43] J. Zhang, N. Kong, S. Uzun, A. Levitt, S. Seyedin, P. A. Lynch, S. Qin, M. Han, W. Yang, J. Liu, X. Wang, Y. Gogotsi, J. M. Razal, *Adv. Mater.* **2020**, *32*, 2001093.
[44] M. K. Shin, B. Lee, S. H. Kim, J. A. Lee, G. M. Spinks, S. Gambhir, G. G. Wallace, M. E. Kozlov, R. H. Baughman, S. J. Kim, *Nat. Commun.* **2012**, *3*, 650.
[45] D. Papkov, N. Delpouve, L. Delbreilh, S. Araujo, T. Stockdale, S. Mamedov, K. Maleckis, Y. Zou, M. N. Andalib, E. Dargent, V. P. Dravid, M. V. Holt, C. Pellerin, Y. A. Dzenis, *ACS Nano* **2019**, *13*, 4893.
[46] S. Wan, Y. Chen, S. Fang, S. Wang, Z. Xu, L. Jiang, R. H. Baughman, Q. Cheng, *Nat. Mater.* **2021**, *20*, 624.
[47] S. Luo, T. Liu, S. M. Benjamin, J. S. Brooks, *Langmuir* **2013**, *29*, 8694.
[48] J. Gao, Y. L. Loo, *Adv. Funct. Mater.* **2015**, *25*, 105.
[49] D. Kang, P. V. Pikhitsa, Y. W. Choi, C. Lee, S. S. Shin, L. F. Piao, B. Park, K. Y. Suh, T. I. Kim, M. Choi, *Nature* **2014**, *516*, 222.
[50] J. Zhou, X. Xu, Y. Xin, G. Lubineau, *Adv. Funct. Mater.* **2018**, *28*, 1705591.
[51] Y. Fang, Y. Zou, J. Xu, G. Chen, Y. Zhou, W. Deng, X. Zhao, M. Roustaei, T. K. Hsiai, J. Chen, *Adv. Mater.* **2021**, *33*, 2104178.
[52] K. L. Van Aken, M. Beidaghi, Y. Gogotsi, *Angew. Chem., Int. Ed.* **2015**, *54*, 4806.
[53] X. Gao, X. Du, T. S. Mathis, M. Zhang, X. Wang, J. Shui, Y. Gogotsi, M. Xu, *Nat. Commun.* **2020**, *11*, 6160.
[54] J. Segalini, B. Daffos, P. L. Taberna, Y. Gogotsi, P. Simon, *Electrochim. Acta* **2010**, *55*, 7489.
[55] S. Seyedin, E. R. S. Yanza, J. M. Razal, *J. Mater. Chem. A* **2017**, *5*, 24076.
[56] D. Yu, K. Goh, H. Wang, L. Wei, W. Jiang, Q. Zhang, L. Dai, Y. Chen, *Nat. Nanotechnol.* **2014**, *9*, 555.
[57] B. JWang, X. Fang, H. Sun, S. He, J. Ren, Y. Zhang, H. Peng, *Adv. Mater.* **2015**, *27*, 7854.
[58] G. Sun, X. Zhang, R. Lin, J. Yang, H. Zhang, P. Chen, *Angew. Chem., Int. Ed.* **2015**, *54*, 4651.
[59] P. Shi, L. Li, L. Hua, Q. Qian, P. Wang, J. Zhou, G. Sun, W. Huang, *ACS Nano* **2017**, *11*, 444.
[60] D. Yu, S. Zhai, W. Jiang, K. Goh, L. Wei, X. Chen, R. Jiang, Y. Chen, *Adv. Mater.* **2015**, *27*, 4895.
[61] Z. Yu, J. Thomas, *Adv. Mater.* **2014**, *26*, 4279.
[62] J. Zhang, S. Seyedin, S. Qin, Z. Wang, S. Moradi, F. Yang, P. A. Lynch, W. Yang, J. Liu, X. Wang, J. M. Razal, *Small* **2019**, *15*, 1804732.
[63] C. Yu, Y. Gong, R. Chen, M. Zhang, J. Zhou, J. An, F. Lv, S. Guo, G. Sun, *Small* **2018**, *14*, 1801203.
[64] X. Zhou, Y. Qin, X. He, Q. Li, J. Sun, Z. Lei, Z. Liu, *ACS Appl. Mater. Interfaces* **2020**, *12*, 11833.

© 2023 Wiley-VCH GmbH

15214095, 2023, 15, Downloaded from https://onlinelibrary.wiley.com/doi/10.1002/adma.202209527 by Nankai University, Wiley Online Library on [14/05/2023]. See the Terms and Conditions (https://onlinelibrary.wiley.com/terms-and-conditions) on Wiley Online Library for rules of use; OA articles are governed by the applicable Creative Commons License